ARTICLE IN PRESS

Catalysis Today xxx (xxxx) xxx–xxx

Contents lists available at ScienceDirect

Catalysis Today

journal homepage: www.elsevier.com/locate/cattod

Dual origins of photocatalysis: Light-induced band-gap excitation of zirconium oxide and ambient heat activation of gold to enable $^{13}CO_2$ photoreduction/conversion

Hongwei Zhang[a], Takaomi Itoi[b], Kaori Niki[a], Takehisa Konishi[a], Yasuo Izumi[a,*]

[a] Department of Chemistry, Graduate School of Science, Chiba University, Yayoi 1-33, Inage-ku, Chiba, 263-8522, Japan
[b] Department of Mechanical Engineering, Graduate School of Engineering, Chiba University, Yayoi 1-33, Inage-ku, Chiba, 263-8522, Japan

ARTICLE INFO

Keywords:
CO_2 photoconversion
Zirconium oxide
Gold
Localized surface plasmon resonance
Ambient heat
Extended X-ray absorption fine structure

ABSTRACT

Photoconversion of CO_2 into fuels completes the carbon neutral cycle in a sustainable society. To exclude the contribution of adventitious carbon, monitoring the time course of $^{13}CO_2$ conversion into ^{13}C-fuel is essential, but has been rarely reported. In the present work, a composite of Au nanoparticles with ZrO_2 was found to be effective in converting $^{13}CO_2$ into ^{13}CO at a rate of 0.17 μmol h^{-1} $g_{cat}{}^{-1}$ in the presence of H_2 and UV–vis light. The detected ^{12}CO as a minor byproduct (11.9 %) was identified as due to adsorbed $^{12}CO_2$ from the air. The ^{12}C ratio in the total amount of CO_2 was evaluated based on a $^{13}CO_2$ photoexchange reaction (8.7 %). The discrepancy between these values suggested a slower exchange reaction step between the chemisorption site for CO_2 reduction and the physisorption site for CO_2 compared to the reduction step to CO. Furthermore, based on in-profile kinetic studies using sharp-cut filters and control reactions in the dark, the contribution ratio for CO_2 conversion was determined to be via charge separation at the band-gap of ZrO_2 ($\lambda < 320$ nm): 69 % and via ambient heat ($\frac{1}{2}kT$): 31 %. Localized surface plasmon resonance (LSPR) absorption of Au and infrared absorption in the range of $\lambda > 320$ nm did not promote catalysis. The LSPR absorption was further investigated by Au L_3-edge extended X-ray absorption fine structure analysis. Ambient heat on the Au nanoparticles should have promoted H_2 activation enough, supplying protons to the CO_2 reduction sites over ZrO_2; however, a temperature increase of 26 K on the Au surface was marginal for further H_2 activation. CO_2 photoconversion with added moisture was also attempted; the CO formation rate using ZrO_2 under these conditions was 0.15 μmol h^{-1} $g_{cat}{}^{-1}$. However, 47 % was characterized as ^{12}CO originating from chemisorbed $^{12}CO_2$, and H_2 was also formed at a comparable rate of 0.14 μmol h^{-1} $g_{cat}{}^{-1}$ from a competing reaction. The addition of Au to ZrO_2 was found to suppress CO formation and promote H_2 formation, and Mg^{2+} addition to Au–ZrO_2 effectively suppressed H_2 formation directing to the CO formation.

1. Introduction

The conversion of CO_2 into fuels utilizing sustainable energy sources completes the carbon neutral cycle in an ideal, sustainable society. Solar fuels, in particular, have been identified as promising alternatives to fossil fuels and have thus been widely investigated [1]. However, solar fuel generation from CO_2 is a highly endothermic, unfavorable process [2], and developing a reaction pathway from CO_2 to fuels without the contribution of adventitious carbon is essential for making this approach viable [3]. Zirconium oxide (ZrO_2) has been shown to successfully promote the photoconversion of $^{13}CO_2$ into ^{13}CO, enabled by both ultraviolet (UV) light-induced band-gap excitation and heat-induced promotion effects converted from localized surface plasmon resonance (LSPR) via Ag doping [3].

^{13}C-labeled studies were carried out to confirm $^{13}CO_2$ conversion via gas chromatography-mass spectrometry (GC–MS) analyses.

Abbreviations: EXAFS, extended X-ray absorption fine structure; fcc, face-centered cubic; FTIR, Fourier transform infrared; GC, gas chromatography; HAADF, high-angle annular dark field; HR-TEM, high-resolution transmission electron microscopy; LSPR, localized surface plasmon resonance; MS, mass spectrometry; NMR, nuclear magnetic resonance; PET, polyethene terephthalate; PTFE, polytetrafluoroethene; rpm, rotations per minute; SHE, standard hydrogen electrode; STEM, scanning transmission electron microscopy; TEM, transmission electron microscopy; XRD, X-ray diffraction

* Corresponding author.
E-mail addresses: zhw9590@yahoo.co.jp (H. Zhang), itoi@faculty.chiba-u.jp (T. Itoi), niki@chiba-u.jp (K. Niki), konishi@faculty.chiba-u.jp (T. Konishi), yizumi@faculty.chiba-u.jp (Y. Izumi).

https://doi.org/10.1016/j.cattod.2020.02.040
Received 27 July 2019; Received in revised form 5 February 2020; Accepted 28 February 2020

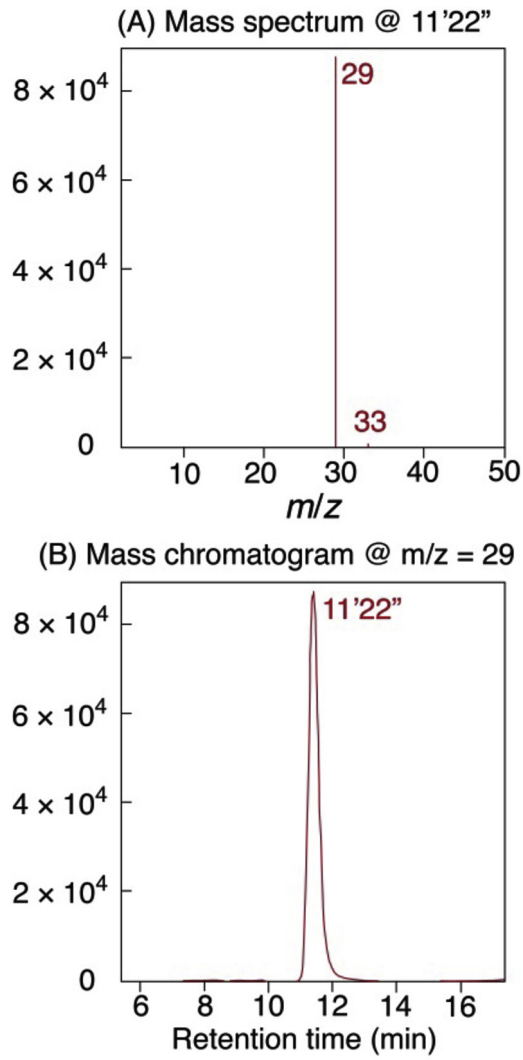

Fig. 1. (A) Mass spectrum @11'22" and (B) mass chromatogram @m/z = 29 sampled during a test under $^{13}CO_2$ (2.3 kPa), H_2 (21.7 kPa), and UV–vis light using the Au (5.0 wt %)–ZrO_2 photocatalyst.

However, very limited data are available in the literature regarding these characterizations: (i) a mass spectrum (Fig. 1A) at a certain retention time in the GC and at only one timepoint during/after the photocatalytic test [4–7], (ii) a mass chromatogram (Fig. 1B) at only one timepoint during/after the photocatalytic test [8,9], and (iii) both a mass spectrum and a mass chromatogram at only one timepoint during/after the photocatalytic test [10–12]. ^{1}H and/or ^{13}C nuclear magnetic resonance (NMR) spectroscopic analyses at one timepoint during/after the photocatalytic test have also been reported [13]. Although such limited data exist, time course monitoring of reactants and products via isotopic labeling, mass chromatography, and/or NMR spectroscopy will be essential for understanding the $^{13}CO_2$ conversion reaction mechanism [3].

The LSPR effects of Au and Ag have been intensively investigated [14]. The resonance peak position is red-shifted for Au in the wavelength of visible light in comparison to that for Ag, promising for use of solar energy [15,16]. In the present work, Au particles were doped into ZrO_2 as a potential catalyst for CO_2 reduction [15–17]. As reductant, H_2 and water were tested [2,18]. Using water, CO_2 reduction and water reduction to H_2 are competitive reactions, and the Mg^{2+} addition to Ag–ZrO_2 photocatalyst was effective to direct to the CO_2 reduction by the anchoring of CO_2 with alkaline [3,19]. The Mg^{2+} addition was also tried to Au–ZrO_2. The reaction progress was monitored via GC–MS analysis, and the photocatalytic role of Au was clarified using Au L_3-edge extended X-ray absorption fine structure (EXAFS) spectroscopy.

2. Experimental section

2.1. Catalyst synthesis/preparation

2.1.1. Au–ZrO_2

ZrO_2 (JRC-ZRO-3, Catalysis Society of Japan; major monoclinic and minor tetragonal phase, specific surface area = 94.4 $m^2\ g^{-1}$) powder was immersed in 50 mL of purified water (< 0.055 μS cm^{-1}), and hydrogen tetrachloroaurate trihydrate (> 99 %, Wako Pure Chemical, Japan; 0.064 or 0.11 g, 0.16 or 0.28 mmol) was added into the suspension. The mixture was agitated by ultrasound (430 W, 38 kHz) for 10 min and magnetically stirred at a rate of 900 rotations per minute (rpm) for 2 h. Sodium borohydride (> 95 %, Wako Pure Chemical; 1.9 or 3.4 mmol) dissolved in purified water (20 mL) was added and magnetically stirred at a rate of 900 rpm. Then, the suspension was filtered using a polytetrafluoroethene (PTFE)-based membrane filter (Omnipore JVWP04700, Millipore, Burlington, MA, USA; pore size 0.1 μm) and washed by purified water (50 mL) five times. The resultant powder was dried at 373 K overnight. The obtained purple powder is denoted as Au–ZrO_2. The loading of Au was 3.0 and 5.0 wt %.

2.1.2. Mg–Au–ZrO_2

Au (5.0 wt %)–ZrO_2 (0.20 g) and magnesium nitrate hexahydrate (2.6 mg, > 99.5 %, Wako Pure Chemical) were mixed in 30 mL of purified water and agitated by ultrasound. The water was distilled and the resultant powder was dried at 373 K overnight. The obtained purple powder is denoted as Mg–Au–ZrO_2. The molar ratio of Mg:Au was 1:5.

2.2. Photocatalytic conversion of $^{13}CO_2$

The photocatalyst (0.100 g) was placed in a quartz photoreactor and evacuated at 295 K for 2 h while connected to a Pyrex glass circulation system (206.1 mL) and both rotary and diffusion pumps (10^{-6} Pa) [2,15,20]. For $^{13}CO_2$ photoexchange tests, 0.67 kPa of $^{13}CO_2$ (^{13}C 99.0 %, ^{17}O 0.1 %, ^{18}O 0.7 %, chemical purity > 99.9 %, Cambridge Isotope Laboratories, Inc., Tewksbury, MA, USA) were introduced (test i) [3]. For $^{13}CO_2$ photoreduction tests, 2.3 kPa of $^{13}CO_2$ and 21.7 kPa of H_2 (> 99.99 %) were introduced (test ii) [3,20]. Separately, 2.3 kPa of $^{13}CO_2$ and 2.7 kPa of H_2O were introduced for $^{13}CO_2$ photoconversion tests using water as the reductant (test iii) [3]. For tests i–iii, the reactor containing the catalyst was irradiated with UV–vis light using a 500 W Xe arc lamp (Model OPM2 − 502, Ushio, Japan). The distance between the UV–vis light source and the photocatalyst was 20 mm. The light intensity was 90.2 mW cm^{-2} at the center of the photocatalyst. The intensity wavelength distribution of the Xe arc lamp was measured using a spectroradiometer (Model USR45DA, Ushio, Japan) at a distance of 20 mm from the UV–vis light source [3]. In-profile kinetic data were collected as a function of the light's excitation wavelength by inserting a sharp-cut filter (2.5 mm thick) at the lighthouse (OPM2 − 502) exit. UV32 and L42 (Hoya, Japan) models were used to pass light of wavelengths $\lambda > 320$ nm and $\lambda > 420$ nm, respectively. Control tests with exposure to $^{13}CO_2$, H_2, and no light were performed by completely wrapping the reactor with Al foil. Control tests were also performed with exposure to only H_2 gas and UV–vis light.

A packed column of 13X-S molecular sieves (3 m length, 3 mm internal diameter; GL Sciences, Inc., Japan) for $^{13}CO_2$ photoreduction/conversion tests ii and iii and a packed column of polyethene glycol-6000/Flusin P support column (3 m length, 3 mm internal diameter; GL Sciences, Inc.) for $^{13}CO_2$ exchange tests i were employed for online GC–MS analyses (Model JMS-Q1050GC, JEOL, Tokyo, Japan). Helium (purity > 99.9999 %) was used as the carrier gas at 0.40 MPa. 4 mL of sampling loops composed of a Pyrex glass system were kept under vacuum using rotary and diffusion pumps (10^{-6} Pa) connected to the

GC–MS via 1.5 m deactivated fused silica tubes (No. 160-2845-10, Agilent, Santa Clara, CA, USA; internal diameter 250 μm), which were maintained at 393 K during analysis to avoid gas adsorption.

2.3. Characterizations

The surface species were monitored with a single-beam Fourier transform infrared (FTIR) instrument (JASCO, Tokyo, Japan; Model FT/IR-4200) equipped with a mercury–cadmium–tellurium-M detector at a constant temperature of 77.4 K. A 20 mm-Φ self-supporting disk of Au (5.0 wt %)–ZrO_2 disk (65 mg) was placed in a quartz photoreaction cell equipped with NaCl windows on both sides. The photoreaction cell was connected to the Pyrex glass circulation system as well as the GC–MS to enable simultaneous monitoring of surface species via FTIR and isotope distribution in the gas with the GC–MS. The photocatalyst disk was evacuated (10^{-6} Pa) at 295 K for 2 h prior to FTIR and GC–MS measurements.

In situ FTIR measurements were performed at 295 K in a range from 4000 to 650 cm^{-1}. The sample disk was irradiated with UV–vis light from a 500 W Xe arc lamp using a quartz fiber light guide (Optel, Tokyo, Japan; Model 1.2S15-1000F-1Q7-SP-RX(400)). The distance between the fiber light exit and sample disk was 46 mm. The light intensity at the center of sample was 90 mW cm^{-2}. The spectrometer's energy resolution was 1 cm^{-1}. Data accumulation was 512 scans (approximately 2 s per scan).

X-ray diffraction (XRD) patterns were observed using a D8 ADVANCE diffractometer (Bruker, Billerica, MA, USA) at the Center for Analytical Instrumentation, Chiba University, at a Bragg angle (θ_B) of $2\theta_B$ = 10–60° with a scan step of 0.02° and a scan rate of 1 s per step. The measurements were performed at 40 kV and 40 mA using Cu Kα emission (wavelength λ = 0.15419 nm) [21] and a nickel filter. Crystallite sizes (t) were estimated using the Scherrer equation [16,22].

$$t = \frac{0.9\lambda}{\text{Peak width} \times \cos\theta_B} \tag{1}$$

UV–visible spectra were recorded on a double-beam model V-650 spectrophotometer using D_2 and halogen lamps below and above 340 nm equipped with a photomultiplier tube and an integrated ISV-469 sphere (JASCO, Tokyo, Japan) for diffuse-reflectance detection within the wavelength range of 200–800 nm. Data were transformed using the Kubelka–Munk function. A PTFE plate was used as the references [3,15,20].

Au L_3-edge EXAFS spectra were measured at 290 K in transmission mode at the Photon Factory Advanced Ring, High Energy Accelerator Research Organization (KEK, Tsukuba, Japan) on the NW10A beamline and also at the Photon Factory, KEK on the 9C beamline [15,16]. On the NW10A beamline, a Si(3 1 1) double-crystal monochromator and a Pt-coated focusing bent cylindrical mirror were inserted into the X-ray beam path. On the 9C beamline, a Si(1 1 1) double-crystal monochromator and Rh-coated focusing bent cylindrical mirror were inserted into the X-ray beam path. On both beamlines, a Piezo transducer was used to detune the X-ray to two-thirds of the maximum intensity to suppress higher harmonics. The Au L_3-edge absorption energy was calibrated at 11 921.2 eV [23] using the X-ray spectrum of a Au metal foil (6 μm thick).

A disk (Φ = 10 mm) of the Au (5.0 wt %) − ZrO_2 photocatalyst (80 mg) was set in a Pyrex glass reactor equipped with a Kapton film (Dupont, Wilmington, DE, USA; 50 μm thick) for X-ray transmission and a polyethene terephthalate (PET) film (Teijin, Japan, G2; 50 μm thick) for both UV–vis light and X-ray transmission. The reactor was filled with 2.3 kPa of CO_2 and 21.7 kPa of H_2. The sample was irradiated with UV–vis light from a Xe arc lamp through the PET film at the beamline. X-rays transmitted the disk perpendicularly while incident angle of UV–vis light was 45°. The distance between the light exit of quartz fiber light guide and the sample was 5 cm. The obtained Au L_3-edge EXAFS data were analyzed using the XDAP software package [24]. The pre-edge background was approximated with a modified Victoreen function:

$$\frac{C_2}{E^2} + \frac{C_1}{E} + C_0 \tag{2}$$

where E is the photon energy. The background for post-edge oscillation, μx, was approximated with a smoothing spline function and was calculated for a particular number of data points:

$$\sum_{i=1}^{\text{Data Points}} \frac{(\mu x_i - \text{background}_i)^2}{\exp(-0.075k_i^2)} \leq \text{smoothing factor} \tag{3}$$

where k is the angular photoelectron wavenumber.

Multiple-shell curve-fit analyses were performed on the Fourier-filtered k^3-weighted EXAFS data in k- and R-space (R: interatomic distance) based on the plane-wave approximation for amplitude $A_i(k)$, coordination number N_i, backscattering amplitude f_i, Debye–Waller factor σ_i, and mean free photoelectron path λ for shell i using an XDAP code [24],

$$A_i(k) = \frac{N_i}{kR_i^2} |f_i(k)| \exp\left[-2\left(\sigma_i^2 k^2 + \frac{R_i}{\lambda}\right)\right], \text{ i= Au} \tag{4}$$

in which the empirical amplitude extracted from the EXAFS data for the Au_2O_3 powder and Au metal foil (6 μm thick) was used. The R values for the Au–O and Au − Au interatomic pair were set to 0.201 3 nm with an N value of 4 [25] and 0.288 4 nm with an N value of 12, respectively [26]. We assumed that the many-body reduction factor, ${S_0}^2$, was identical for both the sample and reference. The Debye temperature (θ_D, 165 K) was used for bulk Au [27] while a "surface Debye temperature" [$\theta_{D(Surf,\infty)}$] of 83 K was used to account for the motion of vertical freedom of translation of face-centered cubic (fcc) Au(1 1 1) or the (1 1 0) surface [28].

EXAFS analysis was also performed by dividing the amplitude by that of the reference EXAFS data (log-ratio method) using the Athena Demeter package (version 0.9.26) based on the following:

$$\begin{aligned} \ln\frac{A_i(k)}{A_{i,Ref}(k)} &= \ln\frac{N_i}{N_{i,Ref}} - 2(\sigma_i^2 - \sigma_{i,Ref}^2)k^2 + f(R_i, R_{i,Ref}) \\ &\approx \ln\frac{N_i}{N_{i,Ref}} - 2(\sigma_i^2 - \sigma_{i,Ref}^2)k^2 \end{aligned} \tag{5}$$

The EXAFS amplitude of the Au–ZrO_2 photocatalyst before light irradiation was used as the reference $A_{i,Ref}(k)$ data. The k^3-weighted EXAFS function was Fourier transformed and inversely Fourier transformed in a filtered range of 0.20–0.32 nm (phase shift uncorrected) for Au–Au bonds (i = Au in Eq. (5)). Then, the function was fit to data in a k-range of 0–130 nm^{-1} based on Eq. (5).

The sample temperature changes irradiated under UV–vis light were reconfirmed by IR thermography using a model T650sc (FLIR, Wilsonville, OR, USA) equipped with a lens of instantaneous field of view = 25 μm. The position and the incident angle of UV–vis light were common to the conditions for Au L_3-edge EXAFS measurements, but the sample was in ambient air in the IR thermography monitoring.

The transmission electron microscopy (TEM) investigations were performed using a JEM-2100 F (JEOL) equipped with a field emission gun at an acceleration voltage of 200 kV at the Center for Analytical Instrumentation [3,22]. The samples were mounted on Cu mesh (250 mesh per inch) coated with carbon and a copolymer film of poly(vinyl alcohol) and formaldehyde (Formvar, Monsanto, St. Louis, MO, USA). High-angle annular dark-field (HAADF) scanning TEM (STEM) and high-resolution (HR) TEM images were also observed using the JEM-2100 F model. Chemical compositions and elemental distributions were analyzed using energy dispersive spectra equipped with a Si(Li) detector in the TEM.

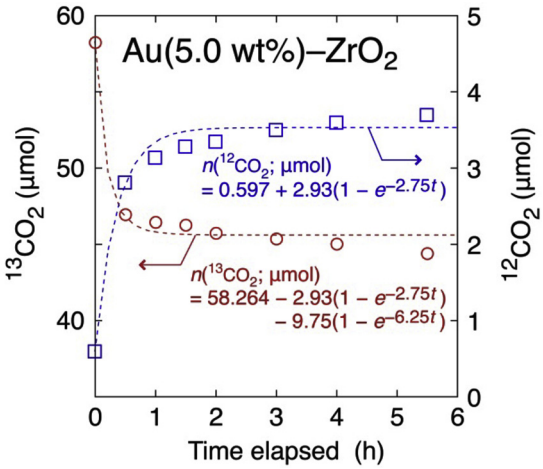

Fig. 2. Time course exchange reaction of $^{13}CO_2$ (0.67 kPa) irradiated by UV–vis light using the Au (5.0 wt %)–ZrO_2 catalyst (0.100 g).

3. Results and discussion

3.1. The $^{13}CO_2$ exchange reaction

We performed a $^{13}CO_2$ (0.67 kPa) exchange reaction with the Au (5.0 wt %)–ZrO_2 photocatalyst under UV–vis light irradiation (Fig. 2). The exchange reaction proceeded with $^{12}CO_2$, which was adsorbed from the atmosphere and remained after pretreatment under vacuum. The exchange reaction reached equilibrium between the adsorbed $^{12}CO_2$ and gas phase $^{13}CO_2$ after 2 h. We assumed that the exchange reaction followed first-order kinetics and that the rate constants, k_r and k_r', corresponded to the exchange reactions between gas-phase $^{13}CO_2$ with adsorbed $^{12}CO_2$ and gas-phase $^{12}CO_2$ with adsorbed $^{13}CO_2$, respectively.

$$\frac{dP_{^{13}CO_2}}{dt} = -k_r P_{^{13}CO_2} + k_r' P_{^{12}CO_2} \quad (6)$$

$$P_{^{13}CO_2} + P_{^{12}CO_2} = P_{^{13}CO_2(\text{initial})} \quad (7)$$

$$P_{^{12}CO_2} = P_{^{12}CO_2\,(\text{equilibrium})}\{1 - e^{-(k_r+k_r')t}\} \quad (8)$$

On the basis of the fit of Eq. (8) to the data of $^{12}CO_2$ evolution (Fig. 2, □), the sum of the rate constants ($k_r + k_r'$) required to attain an exchange equilibrium was 2.8 h^{-1}. The evolution of $^{12}CO_2$ means the uptake of $^{13}CO_2$ on surface with the same equilibrium amount (2.9 μmol) and rate constant (2.8 h^{-1}; Fig. 2, ○). Furthermore, a simple adsorption reaction of 9.8 μmol $^{13}CO_2$ along the free sites of the ZrO_2 surface was substantially faster than $^{13}CO_2/^{12}CO_2$ exchange (2.9 μmol) with a rate constant of 6.3 h^{-1}. The converged $^{12}CO_2$ partial pressure based on total CO_2 was 8.7 %.

3.2. Photoconversion in CO_2 and H_2

The ZrO_2 and Au–ZrO_2 photocatalysts selectively formed CO in the presence of $^{13}CO_2$ and H_2 (Fig. 3A). Using ZrO_2 as the catalyst, ^{13}CO and ^{12}CO were formed at the same rates (0.018 μmol h^{-1} g_{cat}^{-1}), which were constant for more than 50 h of reaction time (Table 1A-a and Fig. 3A-a). In the $^{13}CO_2$ (0.67 kPa) exchange reaction with adsorbed $^{12}CO_2$, the converged $^{12}CO_2$ partial pressure based on total CO_2 was 7.3 % for ZrO_2 [3]. During the initial 5 h of the photoreduction reaction, ^{12}CO formation was more favorable compared to ^{13}CO formation, which started after 1.5 h of reaction time (Fig. 3A-a, Left panel). This observation suggests that the ^{12}CO source was actually pre-adsorbed $^{12}CO_2$ on ZrO_2 from the atmosphere. The exchange equilibrium between adsorbed $^{12}CO_2$ at the photoreduction site of ZrO_2 (CO_2-chemisorbed site) and $^{13}CO_2$ in the gas phase should be slower (Scheme 1-ii, iii) than C—O bond dissociation reaction of CO_2 to form CO (Scheme 1-iii, vi), and thus the ^{12}CO ratio of the total CO formed did not reach the equilibrium isotope ratio of $^{13}CO_2$: $^{12}CO_2$ (7.3 %) [3].

Using Au (3.0 wt %)–ZrO_2 as the photocatalyst, the formation rates of ^{13}CO and ^{12}CO were constant for 30 and 48 h, respectively (Fig. 3A-b, Right panel). Between 30 and 50 h of reaction time, the ^{13}CO formation rate decreased by 5.5 %. The initial constant formation rates were 0.12 and 0.017 μmol, and the ^{12}CO ratio based on total CO was 12.2 % (Table 1A-b). The ^{12}CO ratio, based on total CO formed using Au (3.0 wt %)–ZrO_2 as the photocatalyst dramatically decreased from the value under ZrO_2 photocatalytic conditions (49.2 %), but did not completely reach the ^{12}C ratio in the exchange equilibrium of CO_2 (7.3 % for ZrO_2 [3] and 8.7 % for Au (5.0 wt %)–ZrO_2, Fig. 2). The increase of CO formation rate by a factor of 3.9 times compared to that using ZrO_2 (Table 1A-a, b) suggested the activation of chemisorbed CO_2 species over ZrO_2 in proximity of Au (Scheme 1-iii), facilitating both the transformation from physisorbed to chemisorbed CO_2 species (ii, iii) and further decomposition to CO and H_2O (iii, vi).

The formation rates of ^{13}CO and ^{12}CO were 0.17 and 0.022 μmol h^{-1} g_{cat}^{-1} using Au (5.0 wt %)–ZrO_2 (Table 1A-c), greater by factors of 1.38 and 1.34, respectively, compared to the corresponding values using Au (3.0 wt %)–ZrO_2 (Fig. 3A-b, c). The ^{12}CO ratio in total CO formed was 11.9 %, effectively equivalent to the Au (3.0 wt %)–ZrO_2 conditions (12.2 %, Table 1A-b, c), but still greater than the observed ^{12}C isotopic ratio in the exchange reaction of $^{13}CO_2$ (8.7 %, Fig. 2). The formation rate was constant for ^{13}CO and ^{12}CO for 29 and 48 h of reaction time, respectively, whereas the formation rate of ^{13}CO decreased by 5.0 % after 47 h (Fig. 3A-c, Right panel). The Au (5.0 wt %)–ZrO_2 photocatalyst was most efficient at reducing CO_2 into CO (0.19 μmol h^{-1} g_{cat}^{-1}) in the present work (Table 1A-c). The relatively stable chemisorption site of the photocatalyst (Scheme 1-iii) was an effective photoreduction site for CO_2, and the slower exchange rate between chemisorbed CO_2 and physisorbed CO_2 (Scheme 1-ii, iii) both on ZrO_2 led to minor differences in the ^{12}C isotopic population in formed CO (11.9 %, Table 1A-c) and in equilibrated gaseous CO_2 with the photocatalyst (8.7 %, Fig. 2).

In relation to the reaction mechanism, CO formation rate was as low as 0.004 0 μmol h^{-1} g_{cat}^{-1} in the presence of H_2 (21.7 kPa) and UV–vis irradiation using Au (5.0 wt %)–ZrO_2 photocatalyst (Table 1A-c""). The rate was only 2.1 % of that in the presence of $^{13}CO_2$ and H_2 (Table 1A-c), and the ^{12}CO formation rate was 18 % of the corresponding value in the presence of $^{13}CO_2$ and H_2. Thus, the amount of chemisorbed $^{12}CO_2$-derived species (Scheme 1-iii) decreased in the equilibrium at surface because physisorbed $^{13}CO_2$-derived species (Scheme 1-ii) was absent in the photocatalytic test under H_2 only.

To compare to the photocatalytic reactions under $^{13}CO_2$ and full UV–vis light (Fig. 3A-a–c), studies under a $^{13}CO_2/H_2$ mixture and a UV–vis light filter at λ > 320 nm and at λ > 420 nm were also carried out using the Au (5.0 wt %)–ZrO_2 photocatalyst (Fig. 3A-c', c"). The total CO formation rates decreased by 70 % when using a filter at λ > 320 nm (Table 1A-c, c') and by 78 % when using a filter at λ > 420 nm (Table 1A-c"). The rate difference based on difference in the sharp-cut wavelength was marginal. The formation rates of ^{13}CO and total CO in a control test in the dark (0.050 and 0.055 μmol h^{-1} g_{cat}^{-1}; Table 1A-c''' and Fig. 3A-c''') were essentially identical to the corresponding values in the filtered test at λ > 320 nm (0.052 and 0.055 μmol h^{-1} g_{cat}^{-1}; Table 1A-c'). Thus, visible and IR light were not effective energy sources for the Au–ZrO_2 photocatalysts under CO_2 and H_2. The contribution ratio to CO_2 conversion was charge separation at the band-gap of ZrO_2 (λ < 320 nm): 69 % and ambient heat ($\frac{1}{2}kT$): 31 %.

Unexpectedly, the LSPR absorption of Au (see the following section on UV–vis absorption) and IR absorption for wavelengths λ > 320 nm did not activate H_2 over Au. The decrease of ^{12}CO ratio in total produced CO was evident in the presence of Au (Table 1A-a–c) due to the activation of chemisorbed CO_2 species in the proximity of Au

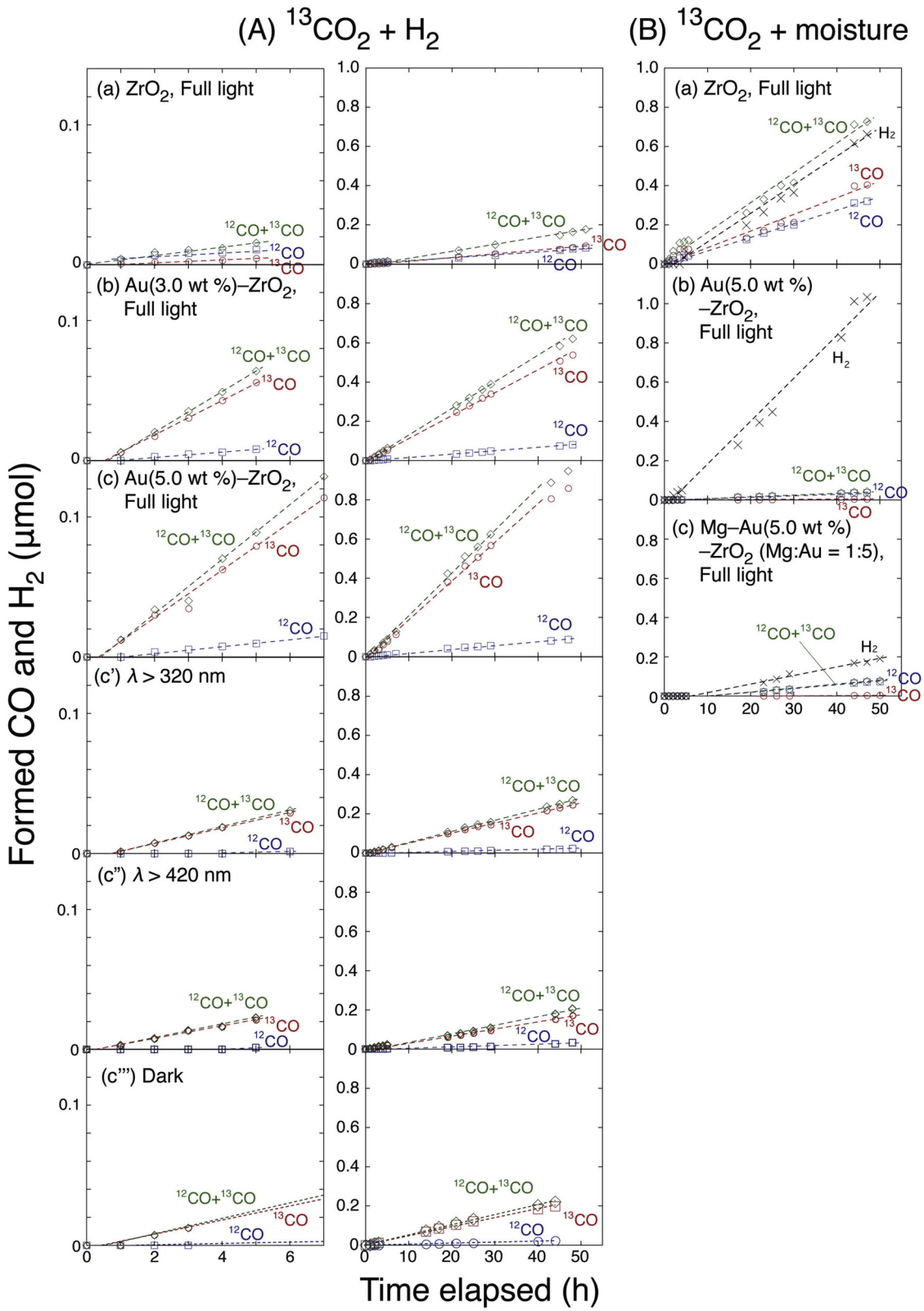

Fig. 3. (A) Time course formation of ^{13}CO and ^{12}CO during exposure to $^{13}CO_2$ (2.3 kPa) and H_2 (21.7 kPa) using (a) ZrO_2 (0.100 g), (b) Au (3.0 wt %)–ZrO_2 (0.100 g), (c) Au (5.0 wt %)–ZrO_2 (0.100 g) irradiated under full UV–vis light, and (c', c", c"') Au (5.0 wt %)–ZrO_2 (0.100 g) irradiated under filtered light at (c') λ > 320 nm and (c") λ > 420 nm and (c"') under dark conditions. (B) Time course formation of ^{13}CO, ^{12}CO, and H_2 during exposure to $^{13}CO_2$ (2.3 kPa) and H_2O (2.3 kPa) using (a) ZrO_2 (0.100 g), (b) Au (5.0 wt %)–ZrO_2 (0.100 g), and (c) Mg–Au (5.0 wt %)–ZrO_2 (0.100 g; Mg:Au = 1:5) irradiated under full UV–vis light.

nanoparticles (Scheme 1-iii). However, the ^{12}CO ratio increased again in the photocatalytic test using a filter at λ > 420 nm (Table 1A-c"), suggesting LSPR effects at Au surface suppressed the activation of chemisorbed CO_2 species. Although spectroscopic evidence is not available for the effects, one possibility is that hot electrons originating from LSPR combined with protons at the interface between Au

Table 1
Kinetic Data on Photoreduction/Conversion of CO_2 using the ZrO_2-Based Photocatalyst under UV–vis Light.

entry	incident wavelength	photocatalyst	formation rate (μmol h^{-1} g_{cat}^{-1})			$^{12}CO/\Sigma CO$ (%)	formation rate (μmol h^{-1} g_{cat}^{-1})
			^{13}CO	^{12}CO	ΣCO		H_2
(A) $^{13}CO_2$ (2.3 kPa) and H_2 (21.7 kPa) except for c"" (H_2 21.7 kPa)							
a	full light	ZrO_2	0.018	0.018	0.036	49.2	–
b		Au (3.0 wt %)–ZrO_2	0.12	0.017	0.14	12.2	–
c		Au (5.0 wt %)–ZrO_2	0.17	0.022	0.19	11.9	–
c'	λ > 320 nm		0.052	0.004 7	0.057	8.3	–
c"	λ > 420 nm		0.034	0.006 2	0.041	15.3	–
c"'	in the dark		0.050	0.004 9	0.055	8.9	–
c""*1	full light		< 0.002	0.004 0	0.004 0	> 95.2	–
(B) $^{13}CO_2$ (2.3 kPa) and H_2O (2.3 kPa)							
a	full light	ZrO_2	0.078	0.068	0.15	46.6	0.14
b		Au (5.0 wt %)–ZrO_2	0.001 5	0.008 5	0.010	85.1	0.23
c		Mg–Au (5.0 wt %)–ZrO_2 (Mg:Au = 1:5)	0.001 6	0.020	0.022	92.6	0.040

*1 Using H_2 only.

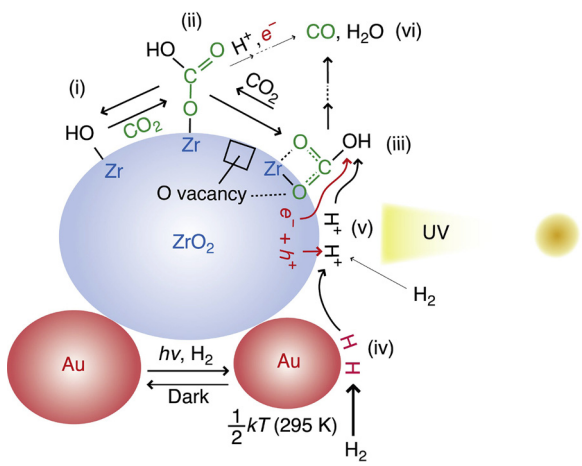

Scheme 1. Proposed reaction pathway (i–vi) for the conversion of CO_2 and H_2 to CO during photocatalytic CO_2 reduction.

nanoparticle and ZrO_2 and directed to H_2 formation as the reverse reaction (Scheme 1-iv, v). Such a negative effect of LSPR is in contradiction to recent progress of the utilization of visible/infrared light [29,30].

It should be noted that the ^{12}CO ratio in total CO formed was 8.3 % using a filter at λ > 320 nm and 8.9 % in the dark (Table 1A-c', c"'), which are effectively the same as that obtained for ^{12}C isotopic population in equilibrated gaseous CO_2 with the photocatalyst (8.7 %, Fig. 2). When the CO formation rates were suppressed (0.055–0.057 μmol h^{-1} g_{cat}^{-1}), the exchange reaction step between physisorbed CO_2 and chemisorbed (and active site) CO_2 was not slow enough to control the overall CO_2 reduction into CO.

3.3. Photoconversion reactions in the presence of CO_2 and moisture

The CO_2 photoconversion with water as the reductant was evaluated in comparison to CO_2 photoreduction with H_2 (Section 3.2). Using ZrO_2 as the catalyst, formation rates of both ^{13}CO and ^{12}CO in the presence of $^{13}CO_2$ and moisture were higher by 4.3 and 3.9 times, respectively, than the corresponding values under $^{13}CO_2$ and H_2 (Table 1A-a and B-a). This result seems contradictory if the latter reaction is regarded as the second step of the former reaction, i.e. water photosplitting and CO_2 reduction with H^+ and e^- (or H_2) [31,32]. In fact, the activation of H_2 was difficult over ZrO_2, whereas water could be activated at the acid–base sites of ZrO_2. The total CO formation rate under these conditions was 0.15 μmol-CO h^{-1} g_{cat}^{-1} (Fig. 3B-a). Furthermore, a competing photoreduction reaction to form H_2 also proceeded at nearly the same rate (0.14 μmol-H_2 h^{-1} g_{cat}^{-1}; Table 1B-a and Fig. 3B-a).

The photocatalytic product distribution drastically changed using Au (5.0 wt %)–ZrO_2 as the photocatalyst (Fig. 3B-b). The CO formation rate was extremely suppressed (6.8 %) when compared to the value using ZrO_2 (Table 1B-a and b). The ^{12}C isotopic ratio among total CO produced increased to 85.1 % in comparison to 46.6 % using ZrO_2. Conversely, the H_2 formation rate increased to 0.23 μmol h^{-1} g_{cat}^{-1}, which was 1.61 times higher than the rate obtained using ZrO_2. O_2 formation was not detected above the detection limit of the GC–MS, suggesting that H_2 formation was associated with the oxygen vacancy site of ZrO_2.

The effects of Mg^{2+} addition on the $^{13}CO_2$ photoconversion reaction were then investigated using a Mg–Au (5.0 wt %)–ZrO_2 catalyst (Table 1B-c). Due to the binding effect of CO_2 by the Mg^{2+} site [3,19], the photocatalysis favored CO_2 reduction rather than H^+ reduction; the H_2 formation rate was suppressed by 83 %, whereas the CO formation rate increased by a factor of 2.17 in comparison to the value using Au (5.0 wt %)–ZrO_2 (Fig. 3B-b, c). However, the molar ratio of CO versus H_2 formation, 0.54: 1, was still smaller in comparison to the ratio obtained when using ZrO_2, 1.02: 1 (Table 1B-a, c).

3.4. Monitoring the surface species during photoconversion of CO_2 and H_2 by FTIR

FTIR spectra were measured for the Au (5.0 wt %)–ZrO_2 pretreated under vacuum (10^{-6} Pa) at 295 K for 2 h. At 2.3 kPa of $^{13}CO_2$ and 21.7 kPa of H_2 for 2 h, peaks at 1588, 1389, and 1220 cm^{-1} appeared (Fig. 4A1) that were assigned to antisymmetric and symmetric stretching vibration of OCO [$\nu_{as(OCO)}$, $\nu_{s(OCO)}$] and bending vibration of OH (δ_{OH}) for bicarbonate (monodentate or bridging) [3,33] and peaks at 1518 and 1304 cm^{-1} also appeared that were assigned to $\nu_{as(OCO)}$ and $\nu_{s(OCO)}$ for carbonate [3,34]. The peak positions were essentially identical to those for ^{13}C-bicarbonate and ^{13}C-carbonate species observed for ZrO_2 and Ag–ZrO_2 [3], demonstrating the formation of these species over ZrO_2 surface.

Corresponding to the spectra in the wavenumber region of 1800–1100 cm^{-1} above, stretching vibration peak of OH (ν_{OH}) for bicarbonate appeared at 3615 cm^{-1} under 2.3 kPa of $^{13}CO_2$ and 21.7 kPa of H_2 (Fig. 4A2). The compensation of ν_{OH} for hydroxy group was not clear due to skewed background level probably due to combinational excitation of IR and visible light [3]. Furthermore, a broad peak appeared at 2905 cm^{-1} in the wavenumber region of 3000–2800 cm^{-1} (Fig. 4A3). This wavenumber is too high as formate species [22,35], and would be due to formed CH_x species and/or CH_x group in

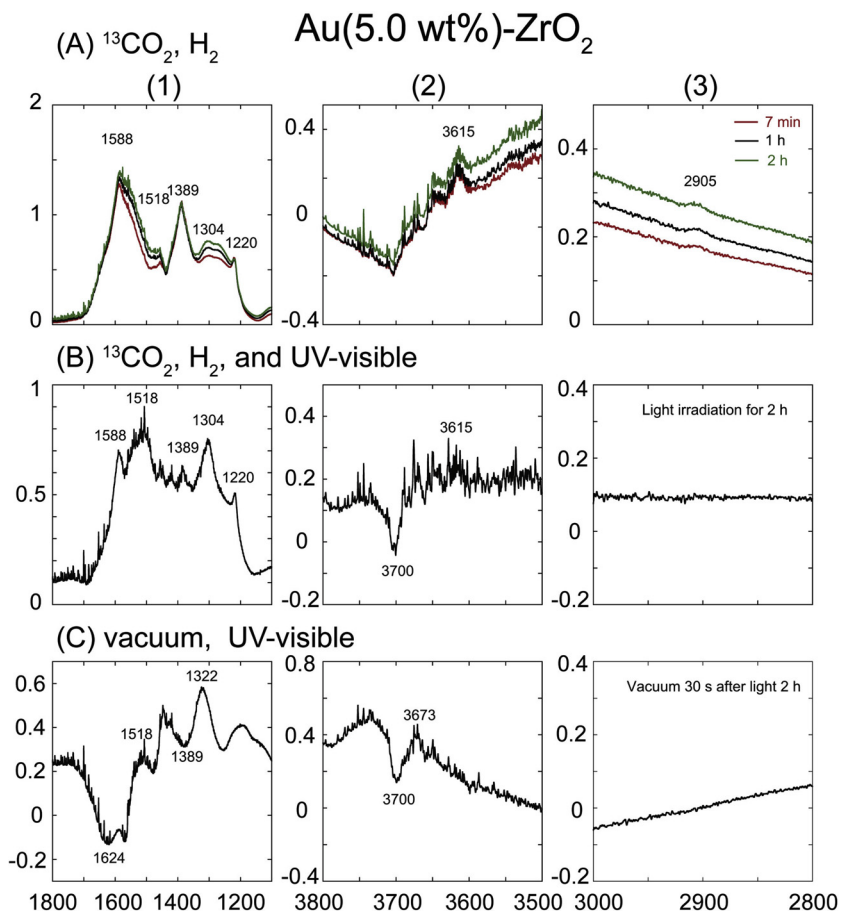

Fig. 4. FTIR spectra of Au (5 wt%)–ZrO_2 (65 mg). (A) Under $^{13}CO_2$ (2.3 kPa) and H_2 (21.7 kPa) for 2 h, (B) Under $^{13}CO_2$ (2.3 kPa), H_2 (21.7 kPa), and UV–vis light for 2 h, and (C) under vacuum and UV–vis light for 2 h.

hydrocarbons.

We then monitored FTIR changes associated with UV–vis light irradiation (Fig. 4B). At 2.3 kPa of $^{13}CO_2$ and 21.7 kPa of H_2 irradiated by UV–vis light for 2 h, peak intensity at 1588 and 1389 cm^{-1} significantly decreased by the effects of UV–vis light, suggesting the conversion of bicarbonate species into CO and/or decomposition to CO_2 and hydroxy group by light. In contrast, peaks at 1518 and 1304 cm^{-1} became prominent (Fig. 4B1) because carbonate species were inert even irradiated under UV–vis light. Accordingly, the ν_{OH} peak intensity at 3615 cm^{-1} due to bicarbonate decreased and negative peak of ν_{OH} for hydroxy group at 3700 cm^{-1} appeared demonstrating that bicarbonate species partially remained. The ν_{CH} peak due to CH_x species/group totally disappeared under irradiation of UV–vis light (Fig. 4B2,3).

During the UV–vis light irradiation for 2 h, we confirmed formations of ^{13}CO and ^{12}CO by GC–MS at rates of 1.8 μmol h^{-1} $g_{cat}{}^{-1}$ and 0.085 μmol h^{-1} $g_{cat}{}^{-1}$, respectively. The decrease of ^{13}C-bicarbonate peak in FTIR and predominant formation of ^{13}CO (95 mol%) by GC–MS suggested the transformation of ^{13}C-bicarbonate into ^{13}CO. In contrast, a broad peak at 2905 cm^{-1} completely disappeared under $^{13}CO_2$, H_2, and UV–vis light (Fig. 4B3), and no C-containing products were detected other than CO above the detection limit of GC–MS, indicating the peak at 2905 cm^{-1} was not related to CO_2 photoconversion in this study.

Later than 2 h of light irradiation, the $^{13}CO_2$ and H_2 gas were evacuated for 30 s at 295 K while the UV–vis light irradiation was continued (Fig. 4C). Negative peaks at 1624 and 1389 cm^{-1} appeared while peaks at 1518 and 1322 cm^{-1} remained. Based on the harmonic oscillation approximation

$$\tilde{\nu} = \frac{1}{2\pi c}\sqrt{\frac{k}{\mu}} \tag{9}$$

$$\frac{\tilde{\nu}_{13CO}}{\tilde{\nu}_{12CO}} = \frac{\sqrt{\frac{1}{13}+\frac{1}{16}}}{\sqrt{\frac{1}{12}+\frac{1}{16}}} = 0.97778 \tag{10}$$

the $\nu_{as(OCO)}$ and $\nu_{s(OCO)}$ peaks for ^{13}C-bicarbonate (1588 and 1389 cm^{-1}) should shift to 1624 and 1421 cm^{-1}, respectively, for ^{12}C-bicarbonate. The discrepancy (32 cm^{-1}) for the wavenumber of $\nu_{s(OCO)}$ peaks would be due to complex overlap of positive and negative FTIR peaks in the region. The ^{12}C-bicarbonte should be chemisorbed from air, but decomposed under vacuum and UV–vis light. Due to the same reason, the wavenumber of $\nu_{s(OCO)}$ peaks (1322 cm^{-1}) assigned to inert ^{13}C-carbonate apparently shifted by 18 cm^{-1} from 1304 cm^{-1} under $^{13}CO_2$ and H_2 (Fig. 4A1, C1) while the $\nu_{as(OCO)}$ peak perfectly remained at the same wavenumber (1518 cm^{-1}). The negative peak at 3700 cm^{-1} and neighboring positive peak at 3673 cm^{-1} (Fig. 4C2) should be due to formed water and/or hydroxy converted from CO_2 and H_2 reduced former isolated hydroxy and increased H-bonded one.

3.5. Characterization by XRD and UV–vis spectroscopy

XRD patterns were collected for the ZrO_2 and Au–ZrO_2 samples. The XRD peaks appeared at $2\theta_B$ = 17.5°, 24.3°, 28.3°, 31.5°, 34.3°, 35.3°, 38.6°, 41.0°, 45.1°, 50.3°, 54.2°, and 55.6° (Fig. 5A), which were ascribed to the 0 0 1, 0 1 1, $\bar{1}$11, 1 1 1, 0 2 0, 0 0 2, 1 2 0, $\bar{1}$12, $\bar{2}$02, 0 2 2, 0 0 3, and 3 1 0 reflections, respectively, of monoclinic ZrO_2 [36,37]. No peaks due to Au metal or Au_2O_3 nanoparticles were observed for the Au (3.0 and 5.0 wt %)–ZrO_2 samples (Fig. 5B, C). In contrast, for the Au nanoparticle samples supported on layered double hydroxide, a Au (111) reflection was reported at $2\theta_B$ = 38.3° [16], suggesting that the Au metal or Au_2O_3 nanoparticles were dispersed and small (< 5 nm)

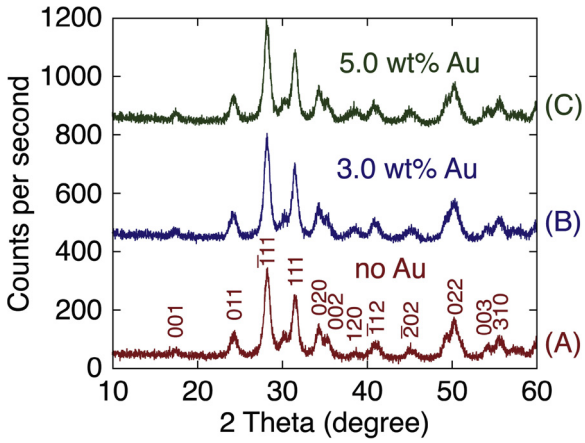

Fig. 5. XRD patterns of the ZrO_2 (A) and Au–ZrO_2 samples (B, C). The Au content was 3.0 (B) and 5.0 wt % (C).

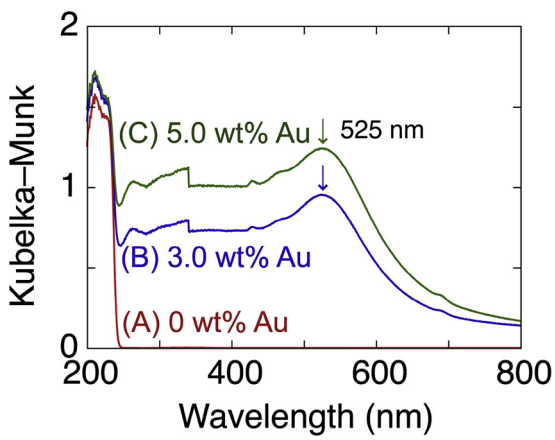

Fig. 6. Diffuse-reflectance UV–vis spectra for ZrO_2 (A) and Au–ZrO_2 samples (B, C). The Au content was 3.0 (B) and 5.0 wt % (C).

enough for this study.

UV–visible spectra were measured for the ZrO_2 and Au–ZrO_2 samples (Fig. 6). A sharp absorption edge appeared at the same position in the UV region for all samples, which was extrapolated to 248 nm from the *x*-axis. The evaluated band-gap value of 5.0 eV for ZrO_2 is consistent with a previous report [3].

The LSPR peak appeared centered at 525 nm for samples doped with 3.0 and 5.0 wt % of Au (arrows in Fig. 6B, C), which is similar to the reported resonance for Au supported on TiO_2 (~550 nm) [38]. Electron transfer from the LSPR Au nanoparticles to the conduction band of TiO_2 within 240 fs was confirmed by transient absorption spectroscopy. In contrast, no transient absorption rise was observed for the Au–ZrO_2 sample, and electron transfer from LSPR Au to the conduction band of ZrO_2 was not detected [39]. Similar to the flat absorption feature that was detected below 450 nm for a colloidal solution of Au nanorods (mean 10 nm), the intermediate absorption between 250 and 450 nm for Au–ZrO_2 (Fig. 6B, C) was due to the intraband electronic transition within Au. Notably, this feature is different from the hot electron transfer from Au to CdSe nanorods [40] because the conduction band of ZrO_2 positions its potential much higher (–1.0 V @standard hydrogen electrode (SHE)) than CdSe (−0.2 V @SHE). The intermediate absorption between 250 and 450 nm detected for Au, the LSPR absorption on Au, and the IR absorption all negligibly contributed to the CO_2 photoreduction (Table 1A-c', c''').

3.6. Characterization by TEM

The TEM image for the Au (5.0 wt %)–ZrO_2 sample is shown in Fig. 7A. Relatively dark spherical images were found and the size was between 2 and 7 nm. Darker parts also appeared near the center of the image primarily due to the primary particles being stuck in the direction of the electron injection probe.

High-resolution transmission electron microscopy (HR-TEM) images for the Au (5.0 wt %)–ZrO_2 sample were then measured and showed the formation of various lattice fringes. Intervals between 0.278–0.284 nm were found for 4–6 nm sized nanoparticles (Fig. 7B, D), corresponding to the Au 1 1 0 lattice (theoretically 0.288 nm based on fcc metal) [26]. For the 4 nm nanoparticles (Fig. 7C), narrower intervals between 0.190–0.224 nm were also detected, corresponding to the Au 2 0 0 lattice (theoretically 0.204 nm). Conversely, at the basal part (a relatively light color compared to the Au nanoparticle part) of the sample, which supported the Au nanoparticles, intervals between 0.305–0.314 nm were detected (Fig. 7B–D). Based on the XRD peak position of the monoclinic ZrO_2 phase (Fig. 5) [36,37], the lattices were ascribed to the monoclinic ZrO_2 $\bar{1}11$ lattice.

HAADF-STEM images were also observed for the Au (5.0 wt %)–ZrO_2 photocatalyst. The Au particles were much more emphasized (see the arrows in Fig. 7F) based on the brilliance dependence on

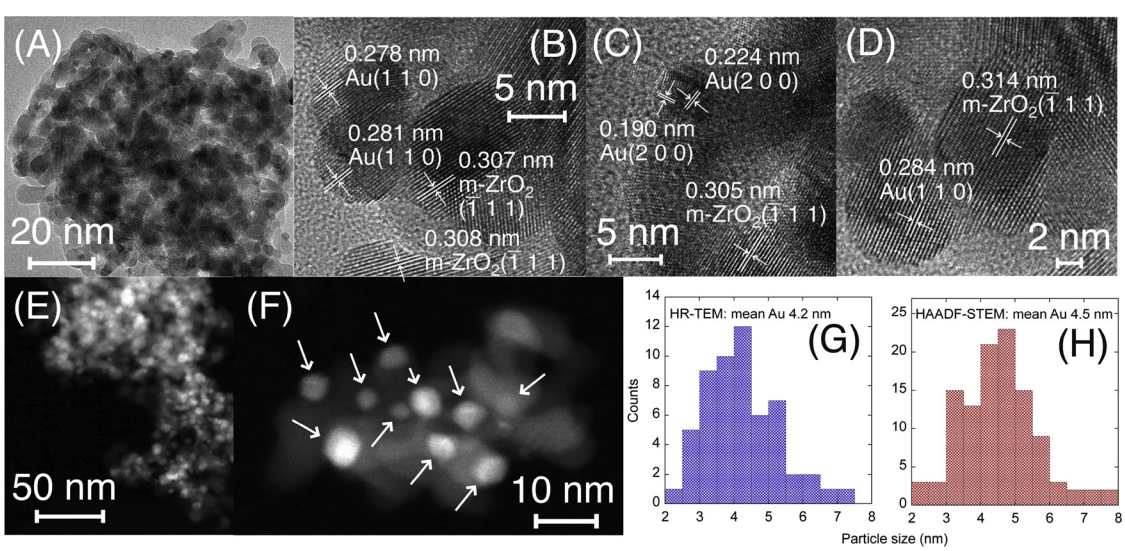

Fig. 7. (A) TEM, (B–D) HR-TEM, and (E, F) HAADF-STEM images for the Au (5.0 wt %)–ZrO_2 photocatalyst and (G, H) the histogram of Au nanoparticle size based on (G) HR-TEM and (H) HAADF-STEM.

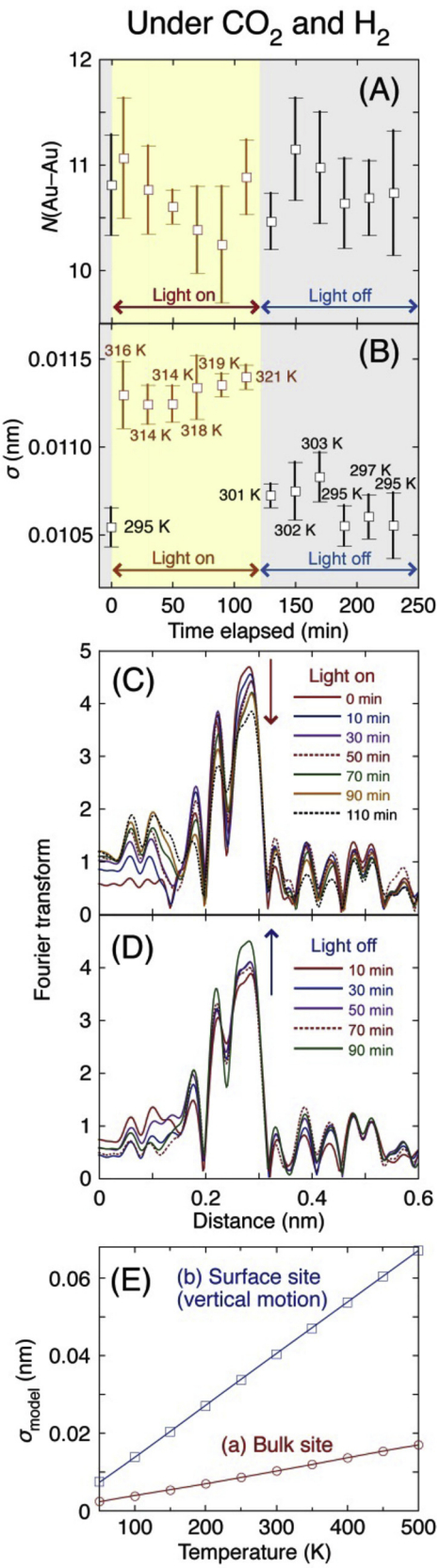

Fig. 8. Time course changes of (A) N values, (B) σ values, and (C, D) Fourier transform obtained from k^3-weighted Au L_3-edge EXAFS χ-function for Au (5.0 wt%)–ZrO_2 under CO_2 (2.3 kPa) and H_2 (21.7 kPa) (C) irradiated by UV–vis light for 120 min followed by (D) dark conditions for 120 min. (E) The correlation between the σ value and temperature for bulk sites (circle, ∘) and surface sites (vertical motion; square, □) in/on the Au metal generated by the correlated Debye model using an FEFF8 code.

atomic number Z^2 (Z for Au 79, Zr 40), and they were positioned on the bundled ZrO_2 nanoparticles (Fig. 7E, F), which is consistent with the HR-TEM images (Fig. 7A–D). The Au nanoparticle size distribution was summarized in the histogram based on HR-TEM and HAADF-STEM analyses (Fig. 7G, H), suggesting a mean size of 4.2 nm and 4.5 nm, respectively.

3.7. In-situ Au L_3-edge EXAFS measurements

Light-induced changes in the Fourier transform function of the EXAFS data were quantitatively evaluated using a curve-fit analysis based on Eq. (4). For the Au (5.0 wt %)–ZrO_2 photocatalyst, the N value was 10.8 ± 0.5 before light irradiation (Fig. 8A), 10.2–11.1 (mean 10.7) during light irradiation, and 10.5–11.1 after the light was turned off (mean 10.8). Based on the mean particle size range of 4.2–4.5 nm obtained for Au in this study (HR-TEM, HAADF-STEM; Fig. 7), the dispersion of the 4.3 nm Au particle was calculated to be 0.31 [41]. The dispersion of Au was thus assumed to be constant at 0.31 in the subsequent analyses.

The σ value was calculated to be 0.009 968 nm for Au metal at 290 K using the correlated Debye model [42,43] with the ab initio multiple-scattering calculation code, FEFF8 [44], and the Debye temperature for Au (165 K) [27]. The XDAP code provides an experimental difference for the σ^2 value from that of the Au metal (model) based on Eq. (4). The initial σ value of 0.010 54 nm for Au (5.0 wt %)–ZrO_2 before light irradiation quickly increased to 0.011 29 nm (10 min light irradiation), remained nearly constant between 0.011 24 and 0.011 34 nm after 70 min of irradiation, and progressively increased to 0.011 40 nm after 110 min of light irradiation (Fig. 8B). Subsequently, this value quickly decreased to 0.010 72 nm after the light was turned off after 120 min of irradiation. The value further decreased gradually to 0.010 55 nm at 190 min, which was essentially the same value as that before light irradiation.

A change in the major peak intensity at 0.24 nm (phase shift uncorrected) was not completely in accord with the change in the σ value during irradiation of UV–vis light for 120 min (Fig. 8B, C). The peak intensity progressively decreased during light irradiation for 110 min, whereas the σ value increased only during the first 10 min but essentially remained constant between 10–110 min of light irradiation. Conversely, the N(Au–Au) value clearly exhibited a decreasing trend during the entire 110 min of light irradiation (Fig. 8A).

To reconfirm the curve-fit analysis results described above, log-ratio method analyses were performed for the EXAFS data of Au (5.0 wt %)–ZrO_2 (Fig. 9). In the log-ratio plots, the y-intercept and slope were related to the N and σ^2 values, respectively, and compared to corresponding values for the reference $A_{i,Ref}(k)$ data before light irradiation based on Eq. (5). During light irradiation (Fig. 9A), the y-intercept remained nearly zero (between −0.07 and 0.04), but it decreased after 30 min and 90 min of photoirradiation, which was similar to the N value decrease detected after 10 min and 90 min via curve-fit analyses (Fig. 8A). Conversely, the slope was also always negative and demonstrated an increase in the σ^2 value compared to the reference value. In stark contrast, after the light was turned off (Fig. 9B), N (y-intercept) values were mostly zero or positive after 30 min of irradiation and the negative σ^2 (slope) values increased, finally reaching zero after 120 min of darkness (Fig. 9B-f). This result demonstrates that these Au nanoparticle features were restored to their original values before light irradiation, which is in agreement with the curve-fit analyses based on Eq. (4) (Fig. 8).

Taken together, the combined effects of the N(Au–Au) and σ value changes resulted in a gradual decrease in the peak intensity at 0.24 nm (phase shift uncorrected), i.e. the initial sudden increase of the σ value and subsequent gradual, slow decrease of the N value.

Furthermore, we evaluated the temperature at the Au site based on the σ values. The temperature dependence of σ value is derived from FEFF8 combined with the correlated Debye model [42,43] for both bulk

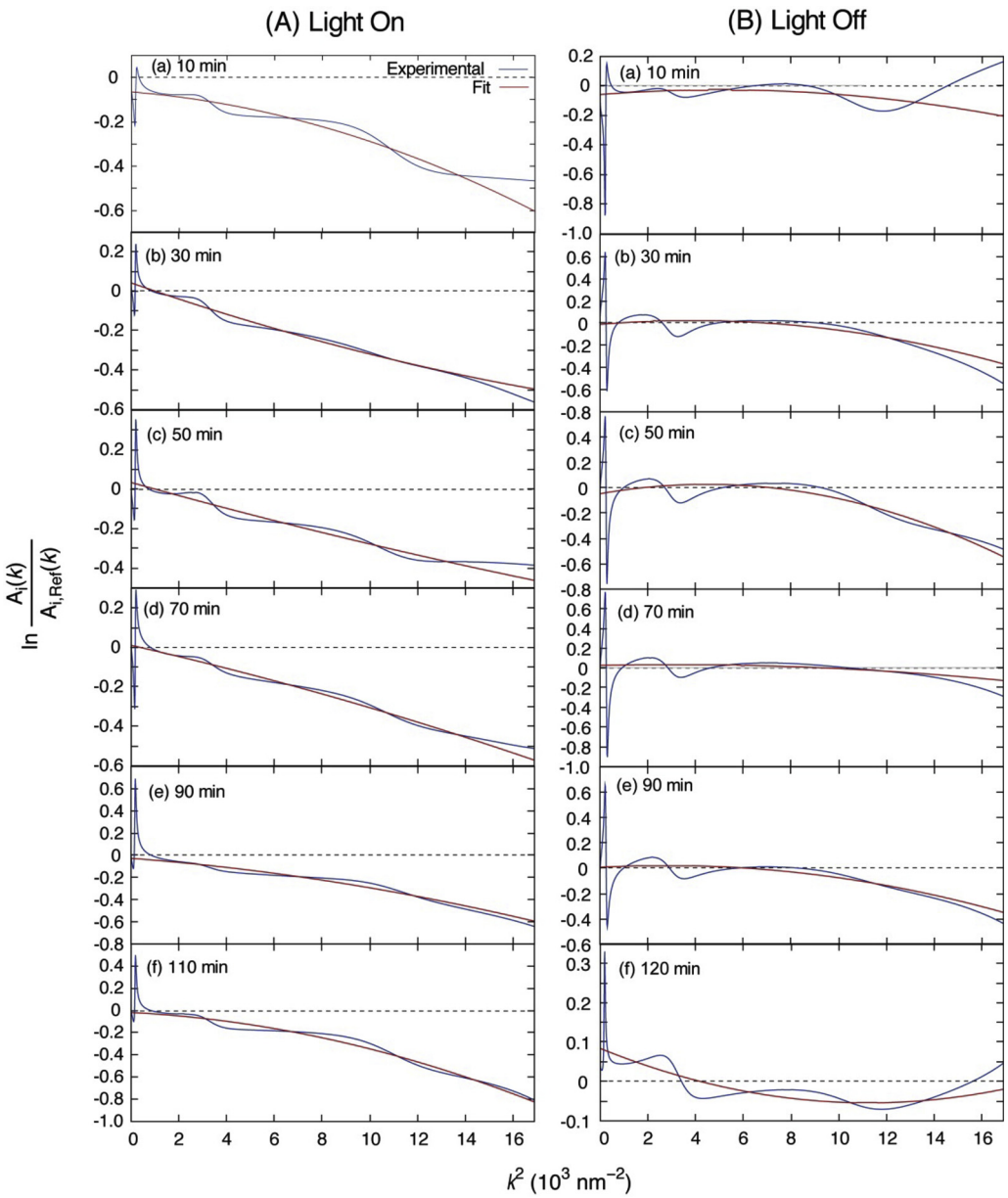

Fig. 9. Log-ratio analyses for EXAFS amplitudes of the Au (5.0 wt %)–ZrO_2 photocatalyst irradiated by UV–vis light (A) and after the light was turned off (B). The changes under light after 120 min (A-a–f) and in the dark for 120 min (B-a–e).

and surface Au sites using the bulk Debye temperature $\theta_{D(Bulk)}$ and surface Debye temperature $\theta_{D(Surf,\perp)}$ (Fig. 8E-a and b, respectively). We assume preferable exposure of thermodynamically stable fcc(1 1 1) or (1 1 0) face for the latter value (83 K) [28]. We also approximated the mean Au nanoparticle temperature as the arithmetic mean temperature based on $\theta_{D(Surf,\perp)}$ weighted by $1/2{\cdot}1/3D$ [D: dispersion of nanoparticles (0.31), for an effective vertical degree of freedom at a free hemisphere surface] and that based on the $\theta_{D(Bulk)}$ weighted by $(1 - D) + 1/2D + 1/2{\cdot}2/3D$ (bulk site, non-free hemisphere in contact with ZrO_2 and two lateral degrees of freedom at a free hemisphere surface).

As a result, the initial temperature of 295 K before light exposure rose to 316 K after 10 min of irradiation, remained nearly constant between 314 and 318 K after 70 min of irradiation, and progressively increased to 321 K after 110 min of light irradiation (Fig. 8B). The temperature quickly dropped to 301 K after the light was turned off. The temperature gradually decreased further to its initial value before light irradiation (295 K) after 190 min. Such rise/drop in temperature is possibly due to LSPR heat transformation [3].

Under the common irradiation conditions of UV–vis light from quartz fiber light guide at 5 cm and incident angle of 45° to the ZrO_2 and Au (5.0 wt %)–ZrO_2 samples (65 mg each), the temperature changes were monitored using IR thermography (Fig. S1, Supplementary material). The temperature of center of light spot on Au–ZrO_2 quickly increased from 295 K to 318 K within less than 1 min and then gradually increased to 328 K at 5 min of irradiation (Fig. S1B) in consistent with the Au temperature change (321 K) monitored by EXAFS (Fig. 8B). In contrast, the temperature of center of UV–vis light spot on ZrO_2 disk increase to only 299 K at 5 min of irradiation (Fig. S1A) and negligible increase was found later than that. Thus, Au nanoparticles absorbed mainly visible light as LSPR resulting in heat for the temperature increase of Au–ZrO_2 sample.

A control EXAFS experiment was performed for the Au (5.0 wt %)–ZrO_2 photocatalyst under Ar and UV–vis light (Fig. 10). The fit parameters, N and σ, followed similar trends to those obtained under CO_2 and H_2 (Fig. 8). The initial N value for light irradiation (11.8) showed a decreasing trend, but the decrease was less than 0.5 and the

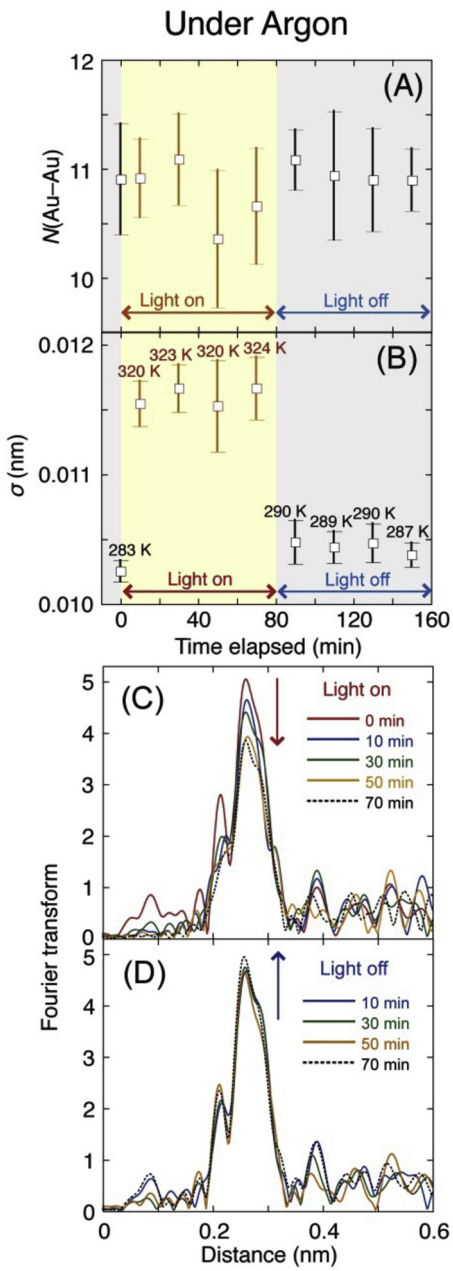

Fig. 10. Time course changes of (A) N values, (B) σ values, and (C) Fourier transform obtained from angular photoelectron wavenumber k^3-weighted Au L_3-edge EXAFS χ-function for Au (5.0 wt%)–ZrO_2 under Ar, (C) irradiated by UV–vis light for 80 min followed by (D) dark conditions for 80 min.

value was restored after the light was turned off (Fig. 10A). Conversely, the initial σ value (0.010 3 nm) rapidly increased after 10 min of light irradiation, remained at high values (~0.011 6 nm) during light irradiation, and quickly dropped to the level before light irradiation in the dark (~0.010 4 nm). Based on the correlated Debye model, the temperature of the Au surface was evaluated to 283 K before light irradiation, 320–324 K during light irradiation, and back down to 290–287 K when the light was turned off (Fig. 10B). The heated temperature range was similarly between 314–321 K under CO_2 and H_2 conditions (Fig. 8B). CO_2 reduction into CO using H_2 as the reductant is an endothermic process ($\Delta_{reaction} H^{\ominus} = 41.16$ kJ mol^{-1}) [3], but the temperature of the system should decrease only by 0.29 mK min^{-1} based on the enthalpy change and the standard heat capacity of ZrO_2 ($C_{p,m}^{\ominus} = 56.123$ J K^{-1} mol^{-1}) and Au ($C_{p,m}^{\ominus} = 25.42$ J K^{-1} mol^{-1}) [45,46]. Thus, the reactant gas did not affect the changes of the N or σ values.

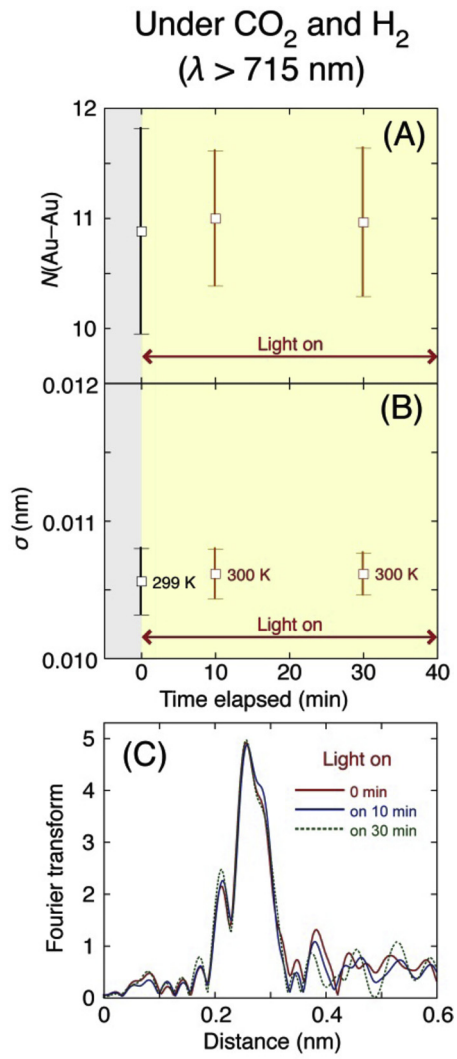

Fig. 11. Time course changes of (A) N values, (B) σ values, and (C) Fourier transform obtained from angular photoelectron wavenumber k^3-weighted Au L_3-edge EXAFS χ-function for Au (5.0 wt%)–ZrO_2 under CO_2 (2.3 kPa) and H_2 (21.7 kPa) irradiated by visible light (> 715 nm) for 40 min.

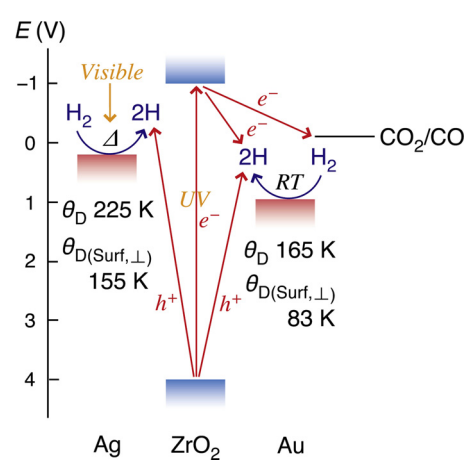

Scheme 2. Energetic diagram of Au or Ag combined with ZrO_2 under CO_2, H_2, and UV–vis light.

The gradual decrease of the Au–Au peak intensity (Fig. 10C) was primarily due to the increase in the σ value and was also associated with the gradual decrease of the N value during light irradiation. As

observed previously, these values were soon restored after the light was turned off (Fig. 10D).

Another control experiment was performed under CO_2 (2.3 kPa) and H_2 (21.7 kPa) conditions using a λ > 715 nm filter. Upon exposure to light for 30 min, no changes in the *N* or *σ* values or the Fourier transform were observed (Fig. 11A–C). Thus, visible light of λ > 715 nm and IR light do not heat the photocatalyst.

An LSPR-induced thermal effect on phenol decomposition has been suggested using Ag nanoparticles on Bi_2WO_6 based on comparisons to control photocatalytic reaction tests conducted at 278–343 K [47]. The conversion of LSPR into heat was monitored using various techniques, including surface-enhanced Raman scattering of Au coated with Pt using *p*-aminothiophenol as the probe molecule [48], Raman scattering of the Au thin films via electric polarization by a 532 nm laser [49], and absorption spectroscopy for Au nanoparticles irradiated by the laser [50].

The energy diagram of Au–ZrO_2 was drawn in comparison to that of Ag–ZrO_2 [3] for CO_2 photoreduction (Scheme 2). The band-gap excitation in ZrO_2 by UV light irradiation generates excited electrons in its conduction band for CO_2 reduction at –0.11 V @SHE [2]. When combined with the Ag nanoparticles, H_2 was effectively activated by LSPR-induced heat at 392 K via the irradiation of visible light. The activated hydrogen was spilled over ZrO_2 and reacted with the hole to form a proton [3] (Scheme 2, left). In stark contrast, Au nanoparticles were disadvantageous for CO_2 photoreduction; the rate under these conditions (0.19 μmol − CO h^{-1} $g_{cat}{}^{-1}$; Table 1A-c) was much slower than the rate obtained using the Ag (5.0 wt %)–ZrO_2 catalyst (0.57 μmol-CO h^{-1} $g_{cat}{}^{-1}$) [3]. This discrepancy is likely due to two major reasons: (i) the heating effect (321 K, Fig. 8B) via LSPR was not sufficient because the Debye temperature was lower for Au (165 K), and thus the heat capacity was greater under UV–vis light in comparison to the Ag (Debye temperature 225 K, enabled 392 K under UV–vis light) (Scheme 2) and (ii) a deeper Fermi level led to collect electrons from the conduction band of ZrO_2 to cancel the hole oxidation of activated H over Au (Scheme 2, right). The reason ii also explains why the light filtered at λ > 320 nm did not contribute to convert CO_2 (Table 1Ac', c", c"').

The promotion mechanism by LSPR has been reported to involve (i) charge excitation to an unoccupied adsorbate state, (ii) hot electron injection that originates from LSPR to the support, (iii) electron trapping from the support to the Schottky barrier, (iv) plasmonic resonant energy transfer, and (v) transformation to heat [3]. Mechanism v was plausible using Ag–ZrO_2, whereas the plasmonic effect was completely hindered by electron injection from the ZrO_2 conduction band to a deeper Au level (Scheme 2, right). The work functions for Au and Ag are significantly different: 5.31–5.47 eV versus 4.52–4.74 eV, respectively [14–18]. In the present work, Au activated H_2 under solely thermal conditions at 295 K to boost photocatalytic CO formation from 0.036 μmol-CO h^{-1} $g_{cat}{}^{-1}$ (ZrO_2) to 0.19 μmol-CO h^{-1} $g_{cat}{}^{-1}$ (Au (5.0 wt %)–ZrO_2 (Table 1A-a, c).

4. Conclusions

The photoexchange reaction under $^{13}CO_2$ revealed that the exchange rate constant between gas-phase CO_2 and chemisorbed CO_2 was 2.8 h^{-1}, whereas adsorption of CO_2 on the free site over ZrO_2 was significantly faster (6.3 h^{-1}). The former site was determined to be the active site for photocatalytic reduction of CO_2 into CO. Au nanoparticles promoted CO_2 photoreduction and Au (5.0 wt %)–ZrO_2 was identified as the most efficient catalyst for CO production at a rate of 0.19 μmol h^{-1} $g_{cat}{}^{-1}$. 11.9 % of ^{12}CO was detected in the product, which is believed to originate from adsorbed $^{12}CO_2$ from the air. It was determined that exchange between chemisorbed and physisorbed CO_2 was slower because the ratio did not reach the equilibrated ratio of $^{13}CO_2$/adsorbed $^{12}CO_2$ in the photoexchange reaction (8.7 %). The CO formation rates using a sharp-cut filter at λ > 320 nm and a control kinetic test in the dark were identical, 0.055 μmol h^{-1} $g_{cat}{}^{-1}$ using Au (5.0 wt %)–ZrO_2, suggesting that the photocatalytic contribution was band-gap charge separation in ZrO_2 (absorption edge 248 nm): 69 % and ambient heat ($\frac{1}{2}kT$): 31 %. H_2 was effectively activated over a Au surface and spilled over H coupled with a hole to form a proton and combined with CO_2 over ZrO_2 to generate CO. The greater work function of Au in comparison to Ag resulted in electron accumulation at Au, which interfered with H spillover and proton formation. The temperature of Au was monitored based on correlated Debye model analysis of EXAFS. The lower Debye temperature of Au (165 K) compared to Ag (225 K) resulted in greater heat capacity and the temperature rise via LSPR was smaller, 26 K under CO_2, H_2, and UV–vis light using Au (5.0 wt %)–ZrO_2 in comparison to 106 K under similar conditions using Ag (5.0 wt %)–ZrO_2. ZrO_2 was effective in promoting both CO and H_2 formation under CO_2, moisture, and UV–vis light conditions, but Au-doped ZrO_2 directed the products toward H_2 production (96 %) via a reverse reaction step. During this pathway, a proton is coupled with an electron, and H_2 formation occurs over the Au surface. The addition of Mg^{2+} to Au–ZrO_2 mitigated the selectivity toward CO, affording 35 % of CO and 65 % of H_2.

Declaration of Competing Interest

I declare no conflict of interest.

Acknowledgments

The authors are grateful for financial support from the Grant-in-Aid for Scientific Research C (17K05961) from the Japan Society for the Promotion of Science, Grant for Academic Research from the Japan Gas Association (2018–2019), and Leading Research Promotion Program (2015–2019) from the Institute for Global Prominent Research, Chiba University. X-ray absorption experiments were performed with the approval of the Photon Factory Proposal Review Committee (2016G577, 2019G141).

Appendix A. Supplementary data

Supplementary material related to this article can be found, in the online version, at doi:https://doi.org/10.1016/j.cattod.2020.02.040.

References

[1] J.H. Hontoya, L.C. Seitz, P. Chakhthranont, A. Vojvodic, T.F. Jaramillo, J.K. Nørskov, Materials for solar fuels and chemicals, Nat. Mater. 16 (1) (2016) 70–81.
[2] Y. Izumi, Recent advances in photocatalytic conversion of carbon dioxide into fuels with water and/or hydrogen using solar energy and beyond, Coord. Chem. Rev. 257 (2013) 171–186.
[3] H. Zhang, T. Itoi, T. Konishi, Y. Izumi, Dual photocatalytic roles of light: charge separation at the band gap and heat via localized surface plasmon resonance to convert CO_2 into CO over silver–zirconium oxide, J. Am. Chem. Soc. 141 (15) (2019) 6292–6301.
[4] X. Wu, Y. Li, G. Zhang, H. Chen, J. Li, K. Wang, Y. Pan, Y. Zhao, Y. Sun, Y. Xie, Photocatalytic CO_2 conversion of $M_{0.33}WO_3$ directly from the air with high selectivity: insight into fill spectrum-induced reaction mechanism, J. Am. Chem. Soc. 141 (13) (2019) 5267–5274.
[5] R. Long, Y. Li, Y. Liu, S. Chen, X. Zheng, C. Gao, C. He, N. Chen, Z. Qi, L. Song, J. Jiang, J. Zhu, Y. Xiong, Isolation of Cu atoms in Pd lattice: forming highly selective sites for photocatalytic conversion of CO_2 to CH_4, J. Am. Chem. Soc. 139 (2017) 4486–4492.
[6] W. Kim, G. Yuan, B.A. McClure, H. Frei, Light induced carbon dixoide reduction by water at binuclear $ZrOCo^{II}$ unit coupled to Ir oxide nanocluster catalyst, J. Am. Chem. Soc. 136 (2014) 11034–11042.
[7] K. Sekizawa, K. Maeda, K. Domen, K. Koike, O. Ishitani, Artificial Z-scheme constructed with a supramolecular metal complex and semiconductor for the photocatalytic reduction of CO_2, J. Am. Chem. Soc. 135 (2013) 4596–4599.
[8] M. Dunwell, Q. Lu, J.M. Heyes, J. Rosen, J.G. Chen, Y. Yan, F. Jiao, B. Xu, The central role of bicarbonate in the electrochemical reduction of carbon dioxide on gold, J. Am. Chem. Soc. 139 (2017) 3774–3783.
[9] T. Yui, A. Kan, C. Saitoh, K. Koike, T. Ibusuki, O. Ishitani, Photochemical reduction of CO_2 using TiO_2: effects of organic adsorbates on TiO_2 and deposition of Pd onto TiO_2, ACS Appl. Mater. Interfaces 3 (2011) 2594–2600.
[10] Y. Wang, Z. Zhang, L. Zhang, Z. Luo, J. Shen, H. Lin, J. Long, J.C.S. Wu, X. Fu,

X. Wang, C. Li, Visible-light driven overall conversion of CO_2 and H_2O to CH_4 and O_2 on 3D-SiC@2D-MoS_2 heterostructure, J. Am. Chem. Soc. 140 (44) (2018) 14595–14598.
[11] H.-C. Hsu, I. Shown, H.-Y. Wei, Y.-C. Chang, H.-Y. Du, Y.-G. Lin, C.-A. Tseng, C.-H. Wang, L.-C. Chen, Y.-C. Lin, K.-H. Chen, Graphene oxide as a promising photocatalyst for CO_2 to methanol conversion, Nanoscale 5 (2013) 262–268.
[12] K. Teramura, S. Iguchi, Y. Mizuno, T. Shishido, T. Tanaka, Photocatalytic conversion of CO_2 in water over layered double hydroxides, Angew. Chem. Int. Ed. 51 (2012) 8008–8011.
[13] L. Wang, M. Ghoussoub, H. Wang, Y. Dong, Y. Shao, A. Tountas, T.E. Wood, H. Li, W. Sun, M. Xia, Y. Li, S. Wang, J. Jia, C. Qiu, C. Qian, L. He, X. Zhang, G.A. Ozin, Photocatalytic hydrogenation of carbon dioxide with high selectivity to methanol at atmospheric pressure, Joule 2 (7) (2018) 1369–1381.
[14] C. Clavero, Plasmon-induced hot-electron generation at nanopaticle/metal-oxide interfaces for photooltaic and photocatalytic devices, Nat. Photonics 8 (2014) 95–193.
[15] S. Kawamura, M.C. Puscasu, Y. Yoshida, Y. Izumi, Tailoring assemblies of plasmonic silver/gold and zinc–gallium layered double hydroxides for photocatalytic conversion of carbon dioxide using UV–visible light, Appl. Catal. A Gen. 504 (2015) 238–247.
[16] G. Mikami, F. Grosu, S. Kawamura, Y. Yoshida, G. Carja, Y. Izumi, Harnessing self-supported Au nanoparticles on layered double hydroxides comprising Zn and Al for enhanced phenol decomposition under solar light, Appl. Catal. B 199 (2016) 260–271.
[17] E.B. Nursanto, H.S. Jeon, C. Kim, M.S. Jee, J.H. Koh, Y.J. Hwang, B.K. Min, Gold catalyst reactivity for CO_2 electroreduction: from nano particle to layer, Catal. Today 260 (2016) 107–111.
[18] Y. Izumi, Recent advances (2012 − 2015) in the photocatalytic conversion of carbon dioxide to fuels using solar energy: feasibility for a new energy, in: F. Jin, L.-N. He, Y.H. Hu (Eds.), Advances in CO − Capture, Sequestration, and Conversion, 1194 ACS Books, Washington, D.C, 2015, pp. 1–46 Chapter 1.
[19] S. Xie, Y. Wang, Q. Zhang, W. Deng, Y. Wang, MgO- and Pt-promoted TiO_2 as an efficient photocatalyst for the preferential reduction of carbon dioxide in the presence of water, ACS Catal. 4 (10) (2014) 3644–3653.
[20] N. Ahmed, Y. Shibata, T. Taniguchi, Y. Izumi, Photocatalytic conversion of carbon dioxide into methanol using zinc–copper–M(III) (M = aluminum, gallium) layered double hydroxides, J. Catal. 279 (2011) 123–135.
[21] Y. Izumi, H. Oyanagi, H. Nagamori, Site-selective X-ray absorption fine structure (XAFS) spectroscopy. (1) design of fluorescence spectrometer and emission spectra, Bull. Chem. Soc. Jpn. 73 (9) (2000) 2017–2023.
[22] Y. Yoshida, T. Itoi, Y. Izumi, Preferential photooxidation of CO in hydrogen across the crystalline face boundary over spheroidal ZnO promoted by Cu ions, J. Phys. Chem. C 119 (37) (2015) 21585–21598.
[23] J.A. Bearden, X-ray wavelengths, Rev. Modern Phys. 39 (1) (1967) 78–124.
[24] M. Vaarkamp, H. Linders, D. Koningsberger, XDAP Version 2.2.7. XAFS Services International, Woudenberg, The Netherlands, 2006.
[25] P.G. Jones, H. Rumpel, E. Schwarzmann, G.M. Sheldrick, Gold(III) oxide, Acta Cryst. B35 (1979) 1435–1437.
[26] S. Fujii, U. Akiba, M. Fujihira, Geometry for self-assembling of spherical hydrocarbon cages with methane thiolates on Au(1 1 1), J. Am. Chem. Soc. 124 (45) (2002) 13629–13635.
[27] D.E. Gray (Ed.), American Institute of Physics Handbook, 3rd ed., McGraw-Hill, New York, 1972, pp. 4–116.
[28] M. Kostelitz, J.L. Domange, Effective surface Debye–Waller temperatures and mean-square displacements for gold from LEED measurements, Solid State Commun. 13 (3) (1973) 241–244.
[29] M.-Q. Yang, M. Gao, M. Hong, G.W. Ho, Visible-to-NIR photon harvesting: progressive engineering of catalysts for solar-powered environmental purification and fuel production, Adv. Mater. 30 (47) (2018) 1802894.
[30] M.-Q. Yang, L. Shen, Y. Lu, S.W. Chee, X. Lu, X. Chi, Z. Chen, Q.-H. Xu, U. Mirsaidov, F.W. Ho, Disorder engineering in monolayer nanosheets enabling photothermic catalysis for full solar spectrum (250–2500 nm) harvesting, Angew. Chem. Int. Ed. 131 (10) (2019) 3109–3113.
[31] H. Zhang, Y. Izumi, Why is water more reactive than hydrogen in photocatalytic CO_2 conversion at higher pressure? Elucidation by means of X-ray absorption fine structure and gas chromatography–mass spectrometry, Front. Chem. 6 (408) (2018) 1–7.
[32] H. Zhang, S. Kawamura, M. Tamba, T. Kojima, M. Yoshiba, Y. Izumi, Is water more reactive than H_2 in photocatalytic CO_a conversion into fuels using semiconductor catalysts under high reaction pressure? J. Catal. 352 (2017) 452–465.
[33] H. Takano, Y. Kirihata, K. Izumiya, N. Kumagai, H. Habazaki, K. Hashimoto, Highly active Ni/Y-doped ZrO_2 catalysts for CO_2 methanation, Appl. Surf. Sci. 388 (2016) 653–663.
[34] A. Solis-Garcia, J.F. Louvier, A. Almendarez, J.C. Fierro, Participation of surface bicarbonate, formate and methoxy species in the carbon dioxide methanation catalyzed by ZrO_2-Supported Ni, Appl. Catal. B 218 (2017) 611–620.
[35] Y. Yoshida, Y. Mitani, T. Itoi, Y. Izumi, Preferable oxidation of carbon monoxide in hydrogen using zinc oxide photocatalysts promoted and tuned adsorbed copper ions, J. Catal. 287 (2012) 190–202.
[36] K.-H. Choi, N. Duraisamy, M.N. Awais, N.M. Muhammad, H.C. Kim, J. Jo, Investigation on switching behavior of ZrO_2 thin film for memory device applications, Mater. Sci. Semiconduct. Proc. 16 (5) (2013) 1285–1291.
[37] S.N. Tkachev, M.H. Manghnani, A. Niilisk, J. Arric, H. Mändar, Micro-raman spectroscopy and X-ray diffraction studies of atomic-layer-deposited ZrO_2 and HfO_2 thin films, J. Mater. Sci. 40 (2005) 4293–4298.
[38] Y. Tian, T. Tatsuma, Mechanisms and applications of plasmon-induced charge separation at TiO_2 films loaded with gold nanoparticles, J. Am. Chem. Soc. 127 (20) (2005) 7632–7637.
[39] A. Furube, L. Du, K. Hara, R. Katoh, M. Tachiya, Ultrafast plasmon-induced electron transfer from gold nanodots into TiO_2 nanoparticles, J. Am. Chem. Soc. 129 (48) (2007) 14852–14853.
[40] K. Wu, J. Chen, J.R. McBride, T. Lian, Efficient hot-electron transfer by a plasmon-induced interfacial charge-transfer transition, Science 349 (6248) (2015) 632–635.
[41] F. Humblot, D. Didillon, F. Lepeltier, J.P. Candy, J. Corker, O. Clause, F. Bayard, J.M. Basset, Surface organometallic chemistry on metals: formation of a stable ≡Sn (n-C_4H_9) fragment as a precursor of surface alloy obtained by Stepwise hydrogenolysis of Sn(n-C_4H_9)$_4$ on a platinum particle supported on silica, J. Am. Chem. Soc. 120 (1) (1998) 137–146.
[42] G. Beni, P.M. Platzman, Temperature and polarization dependence of extended X-ray absorption fine-structure spectra, Phys. Rev. B 14 (1976) 1514–1518.
[43] E. Sevillano, H. Meuth, J.J. Rehr, Extended X-ray absorption fine structure Debye–Waller factors. I. Monoatomic crystals, Phys. Rev. B 20 (1979) 4908–4911.
[44] L. Ankudinov, B. Ravel, J.J. Rehr, S.D. Condradson, Real-space multiple-scattering calculation and interpretation of X-ray absorption near-edge structure, Phys. Rev. B Condens. Matter Mater. Phys. 58 (1998) 7565–7576.
[45] W.M. Haynes (Ed.), CRC Handbook of Chemistry and Physics, 96th eds., CRC Press, Boca Raton, 2015, pp. 4–124.
[46] M.W. Chase Jr., 4th edition, NIST-JANAF Themochemical Tables 9 (1998), pp. 1–1951 J. Phys. Chem. Ref. Data, Monograph.
[47] Z. Zhang, W. Wang, E. Gao, S. Sun, L. Zhang, Photocatalysis coupled with thermal effect induced by SPR on Ag-loaded Bi_2WO_6 with enhanced photocatalytic activity, J. Phys. Chem. C 116 (2012) 25898–25903.
[48] H. Yang, L.-Q. He, Y.-W. Hu, X. Lu, G.-R. Li, B. Liu, B. Ren, Y. Tong, P.-P. Fang, Quantitative detection of photothermal and photoelectrocatalytic effects induced by SPR from Au@Pt nanoparticles, Angew. Chem. Int. Ed. 54 (2015) 11462–11466.
[49] D. Agarwal, C.O. Aspetti, M. Cargnello, M. Ren, J. Yoo, C.B. Murray, R. Agarwal, Engineering localized surface plasmon interactions in gold by silicon nanowire for enhanced heating and photocatalysis, Nano Lett. 17 (2017) 1839–1845.
[50] C.-W. Yen, M.A. El-Sayed, Plasmonic field effect on the hexacyanoferrate (III)-thiosulfate electron transfer catalytic reaction on gold nanoparticles: electromagnetic or thermal? J. Phys. Chem. C 113 (45) (2009) 19585–19590.